International Journal of Thermal Sciences 135 (2019) 285–297

Contents lists available at ScienceDirect

International Journal of Thermal Sciences

journal homepage: www.elsevier.com/locate/ijts

Unsteady investigation of the heat ventilation in a box prototype

Badis Bakri[a,b,*], Ahmed Ketata[a], Slah Driss[a], Hani Benguesmia[b], Zied Driss[a], Fareh Hamrit[b]

[a] Laboratory of Electro-Mechanic Systems (LASEM), National School of Engineers of Sfax (ENIS), University of Sfax, B.P. 1173, km 3.5 Road Soukra, 3038, Sfax, Tunisia
[b] Mechanical Engineering Department, Faculty of Technologies, University of M'sila, Algeria

ARTICLE INFO

Keywords:
CFD
Unsteady state
Finite volume
Heat ventilation
Box prototype

ABSTRACT

This paper investigates the unsteady state of the heat ventilation in a box prototype with two holes. The CFD simulations were conducted using ANSYS Fluent 17.0 software, which solves the Navier-Stokes equations in conjunction with the standard k-ω turbulence model and by a finite volume discretization method. The presented results, consisting of the distribution of the velocity fields, the temperature, the total pressure and the turbulent characteristics, are very useful to determine the time required for the heating operation and to shrink the energy consumption of the buildings. The comparison between the founded results affirms that the heating time presents a straight effect on the velocity fields. However, for the temperature, the box prototype requires more time and more energy to warm up. In our application, we confirm that the duration of 30 s is sufficient to allow the heating of the box prototype. Indeed, the numerical results compared using the experimental data developed in our laboratory confirms the validity of the numerical method. The good agreements validate the considered computational method.

1. Introduction

The energy use worldwide is increasing every year. For example, the consumption has more than doubled in the last 40 years. The housing and service sector is one of the largest energy users on the world market. To shrink the energy consumption, the use of efficient systems is very crucial [1,2]. In this context, Driss et al. [3] developed a new system occupied by a solar patio. This system improved the microclimate of the building. In other work, Driss et al. [4] proposed an outlining environment suitable building, to improve the thermal comfort. Rauf and Robert [5] studied the life cycle in a residential building for a life range of 150 years. Premrov et al. [6] considered a timber-frame house, taking into accounts the climate data for three different European cities. Zhang et al. [7] evaluated the overall performance of eight prevalent and proposed models for simulating airflows in enclosed environments. Soni and Aliabadi [8] compared steady-state inspiratory and unsteady flows with an inlet Reynolds number of 319 at an idealized ten-generation bronchial tube model via large-scale CFD simulations. Evergren et al. [9] studied both steady and unsteady flow through a three-generation system of non-symmetric bifurcations, and they confirmed that the steady-state solution is not representative of the unsteady cases. Calay et al. [10] performed a numerical study on the unsteady respiratory airflow dynamics within a human lung based on a three-dimensional asymmetric bifurcation model by computational fluid dynamics method. The numerical results for the resting and maximal exercise breathing conditions indicated that the airflow is strongly dependent on the geometry and Reynolds number. Orhan et al. [11] solved the unsteady Navier-Stokes equations, governing the flow under Boussinesq approximation, with the vorticity-stream function formulation using the finite difference method. The development of the flow and temperature fields following these temperature changes are determined numerically. Beak et al. [12] observed some fluctuation in the overall heat transfer characteristics for a certain time. Ultimately, the radiation was found to augment the heat transfer rate, which led to reduce the time required for the flow to reach the steady state. Zhu et al. [13] studied numerically transient laminar natural convection of air in a tall cavity. The availability of the numerical algorithm was also assessed by considering the natural convection of air in a square cavity which is differentially heated from side walls. Jun et al. [14] demonstrated that the transient temperatures at the heaters may become higher than their steady-state values. The study emphasizes that the transient-stage temperatures at the heaters can exceed the corre-

---

[*] Corresponding author. Laboratory of Electro-Mechanic Systems (LASEM), National School of Engineers of Sfax (ENIS), University of Sfax, B.P. 1173, km 3.5 Road Soukra, 3038, Sfax, Tunisia.

E-mail address: badisbakri@yahoo.fr (B. Bakri).

https://doi.org/10.1016/j.ijthermalsci.2018.09.023
Received 2 April 2018; Received in revised form 4 August 2018; Accepted 17 September 2018
1290-0729/

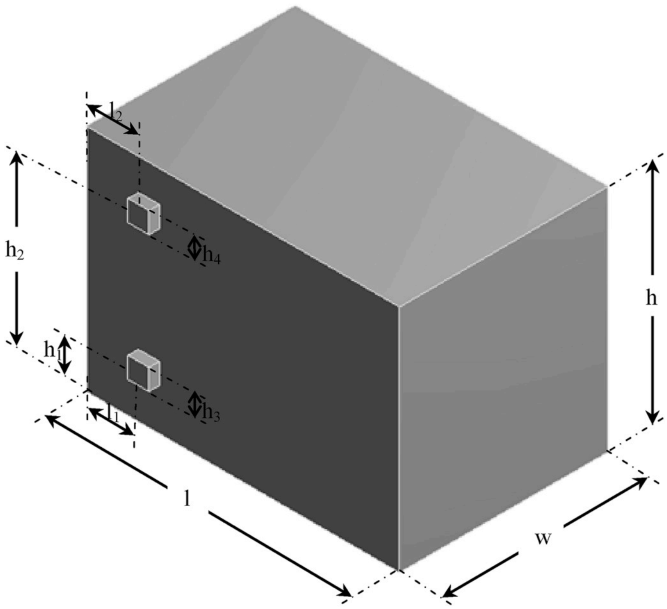

Fig. 1. Geometrical arrangement.

Fig. 2. Anemometer type AM 4204.

Table 1
Characteristics of the anemometer.

Description	Anemometer type AM 4204
Manufacturer	Lutron
Probe type	Telescopic
Measurement parameters	Air velocity, temperature, gaz flow
Resolution	Air velocity 0,1 m s^{-1} Temperature 0,1 °C
Precision	Air velocity 5% Temperature ± 0,8 °C
Measuring range	Air velocity from 0,2–20 m s^{-1} Temperature from −20 °C to +70 °C

Table 2
Standard k-ω turbulence model constants.

α_0	α_∞	α^*_∞	R_ω	R_k	σ_k	σ_ω
1/9	1.9	1.0	2.95	6.0	2.0	2.0

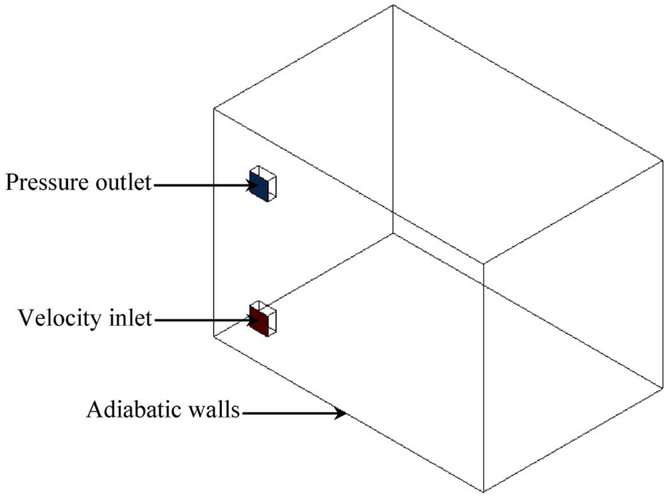

Fig. 3. Boundary conditions.

sponding steady-state values. Irfan et al. [15] study numerically a passive heating room using values of hourly averaged radiation during winter in Elazıg region in Turkey. The effect of the overall heat transfer coefficient of glass on the Nusselt number was also investigated. It was revealed that the overall heat transfer coefficient for low Rayleigh number affected the average Nusselt number more than that of high Rayleigh number. Inna et al. [16] solved numerically the unsteady conjugate natural convection problem in a square enclosure filled with a porous medium having finite thickness heat conducting solid walls at the presence of the internal heat source with constant temperature in conditions of convective–radiative heat exchange with an environment on one of the external borders. Zhang et al. [17] analyzed the back heat transfer and heat transfer resonance phenomena, and their relationships with the time-periodic flow patterns and temperature distributions. The findings are helpful to the understandings of the fluid flow and heat transfer mechanisms in the related enclosure configurations. Semen et al. [18] developed a numerical analysis of transient laminar natural convection and surface radiation in a closed cavity with heat-conducting solid walls of finite thickness and a local heat source of constant temperature in convective heat exchange with an environment. A two-dimensional numerical analysis of combined heat transfer in an air-filled square enclosure having heat-conducting solid walls of finite thickness and a local heat source in conditions of convective heat exchange. Noh-Pat et al. [19] presented a numerical study of the unsteady conjugate heat transfer for a square cavity with a semi-transparent (glass) wall. The cases with or without solar control film on the semitransparent wall were studied from 8:00 to 18:00 h; a time with the multicellular flow than the cavity without film. Armengol et al. [20] studied the effects of variable properties of air in the transient problem of the differentially heated square cavity. The investigation is therefore put forward covering additional effects under regard to the principle of energy conservation, such as the time evolution of the total energy and its components for both transient regime and steady-state cases. Mikhail

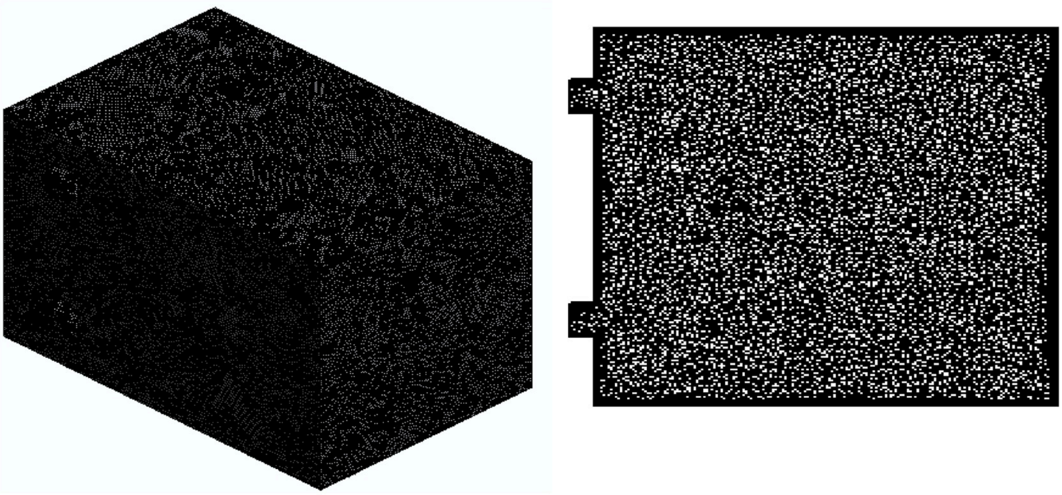

(a) 3D view

(b) 2D view in the plane x= 0.06 m

Fig. 4. Meshing of the computational domain.

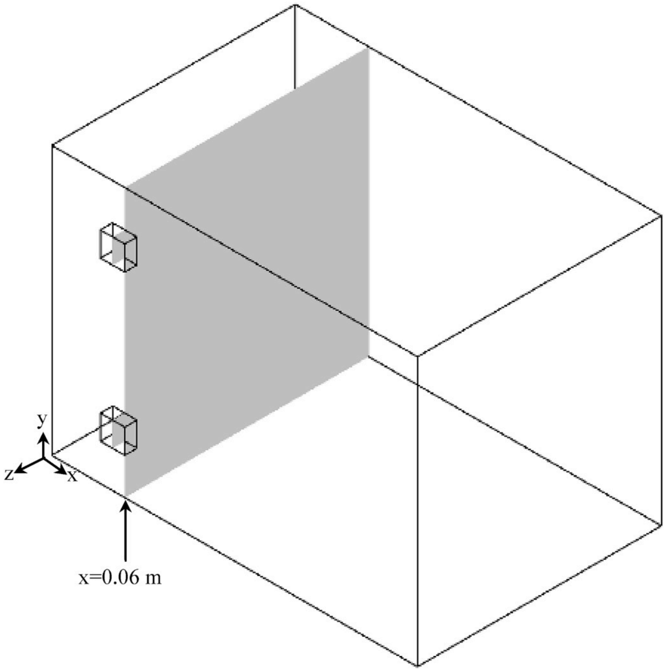

Fig. 5. Visualization plane.

et al. [21] analyzed natural convection of micropolar fluid in a right-angled wavy triangular cavity. The obtained results were illustrated an essential effect of these governing parameters on velocity, temperature and vorticity patterns as well as an average Nusselt number at the hot wavy wall and fluid flow rate. Iker et al. [22] developed a numerical study to obtain turbulent flow and heat transfer for double FFS with different aspect ratios and Reynolds number. The results reveal both turbulent intensity and heat transfer are increased with the increasing of Reynolds number. Fatih et al. [23] investigated numerically the natural convection of ferrofluid in a partially heated square cavity. The effects of a magnetic dipole on the heat transfer enhancement and fluid flow characteristics have been studied in a partially heated cavity. Hakan et al. [24] studied numerically the conjugate heat transfer by mixed convection and conduction in lid-driven enclosures with the thick bottom wall with an enclosure which is heated from the isothermally bottom wall. From the existing literature, it is shown that the investigation of the unsteady CFD simulation of the heat ventilation is a suitable field for further research. The time-dependent outcomes can provide important information, while the temporal variation of indoor temperature and airflow is directly connected to thermal comfort and human life. Also, there are a few types of research on the design method. Therefore, the study of a box prototype was investigated by experimental survey and simulations. An unsteady-state model was implemented using ANSYS software and the results were compared to the experimental results. The present paper is organized as follows. Initially, the examined problem is presented and described and the corresponding conditions are reported. Then the CFD simulation is analyzed and information about the design of the box prototype, the governing equations, the boundary conditions, the numerical procedure and the validation of the model are provided. Subsequently, the results and discussion follow which examine the distribution of the temperature, the velocity fields, the total pressure and the turbulent characteristics. Finally, a number of conclusions are derived providing useful information for similar cases. The results are auspicious and promising.

2. Box prototype system

Fig. 1 presents the geometrical arrangement of the considered box prototype. In this system, the height, the width, and the length are equal to $h = 0.22\,\text{m}$, $w = 0.20\,\text{m}$ and $l = 0.30\,\text{m}$, respectively. In this system, two square holes, with a peak $h_3 = h_4 = 0.02\,\text{m}$, are sited in the same face. From the floor of the box prototype, a first hole, sited at a distance $h_1 = 0.05\,\text{m}$, gives the heated air flow from the outside. From the base, a second hole, sited at a distance $h_2 = 0.18\,\text{m}$, allows the evacuation of the cooled air flow. In practice, the heated air flow comes from a solar air system or from a patio with transparent roofing. As presented by Driss et al. [3], this patio can store the heat energy which is transmitted to the box prototype. To follow the aerodynamic characteristics of the considered box prototype, we measured the temperature and the air velocities in different controlled points. Particularly, we have used the hot-wire anemometer type AM 4204 since it is

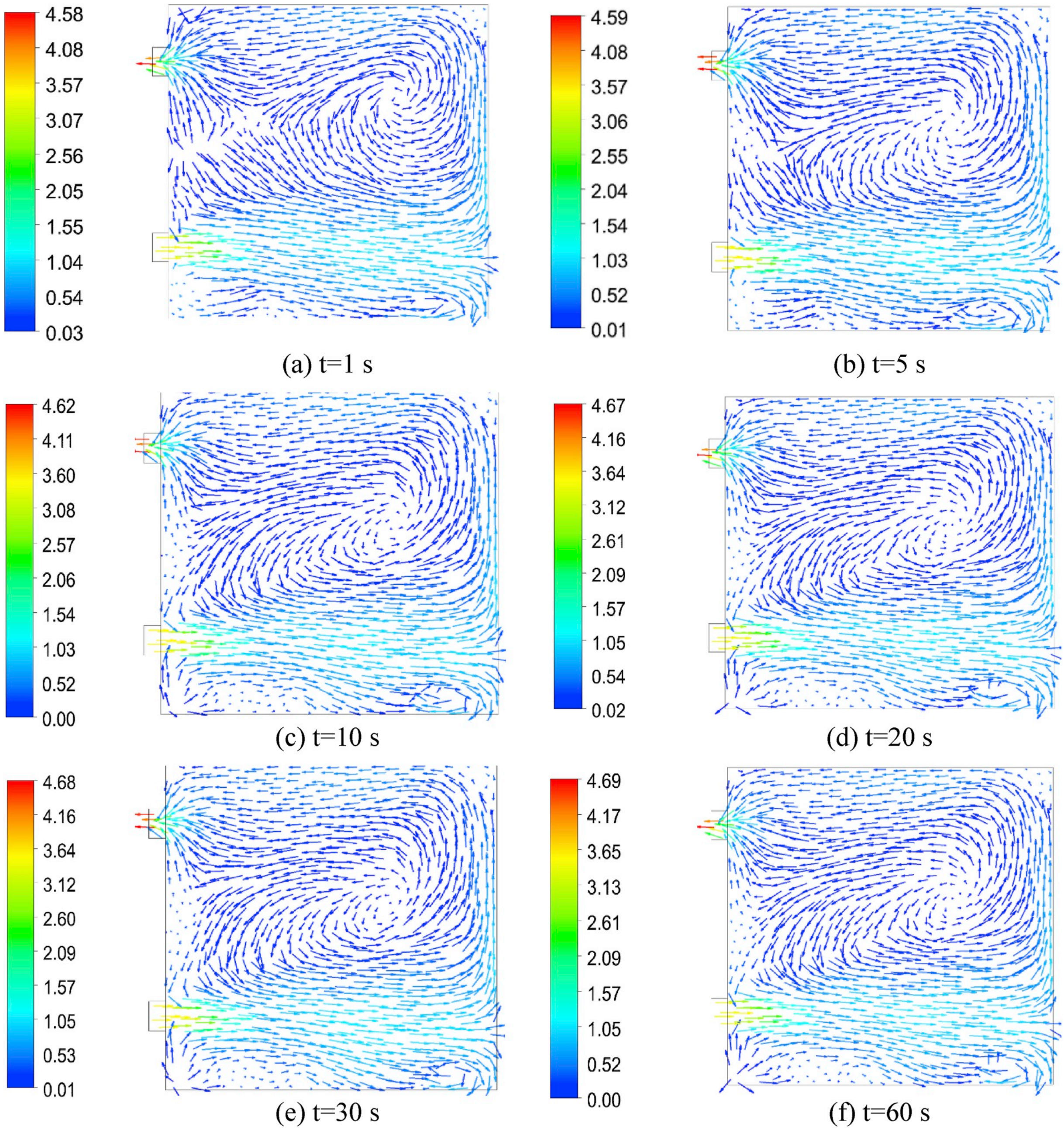

(a) t=1 s

(b) t=5 s

(c) t=10 s

(d) t=20 s

(e) t=30 s

(f) t=60 s

Fig. 6. Velocity fields in the plane defined by x = 0.06 m.

simple and offers the greatest flexibility of use and high-resolution (Fig. 2). The characteristics of the anemometer are summarized in Table 1. By dropping the probe in the appropriate position of the box prototype, the velocity and the temperature values can be read directly from the digital screen.

3. Numerical work

3.1. Governing equations

The air flow modeling is governed by the continuity equation, the momentum equations and the energy equation [25–28]. Substituting expressions into instantaneous equations and taking time average yields, we can write in the Cartesian system:

$$\frac{\partial \rho}{\partial t} + \frac{\partial}{\partial x_i}(\rho\, u_i) = 0 \tag{1}$$

$$\frac{\partial}{\partial\, t}(\rho\, u_i) + \frac{\partial}{\partial\, x_j}(\rho\, u_i\, u_j) = -\frac{\partial\, p}{\partial\, x_i} + \frac{\partial}{\partial\, x_j}\left[\mu\left(\frac{\partial\, u_i}{\partial\, x_j} + \frac{\partial\, u_j}{\partial\, x_i} - \frac{2}{3}\delta_{ij}\frac{\partial\, u_i}{\partial\, x_i}\right)\right] + \frac{\partial}{\partial\, x_j}(-\rho\,\overline{u'_i\, u'_j}) + F_i \tag{2}$$

These equations are the RANS (Reynolds-averaged Navier-Stokes)

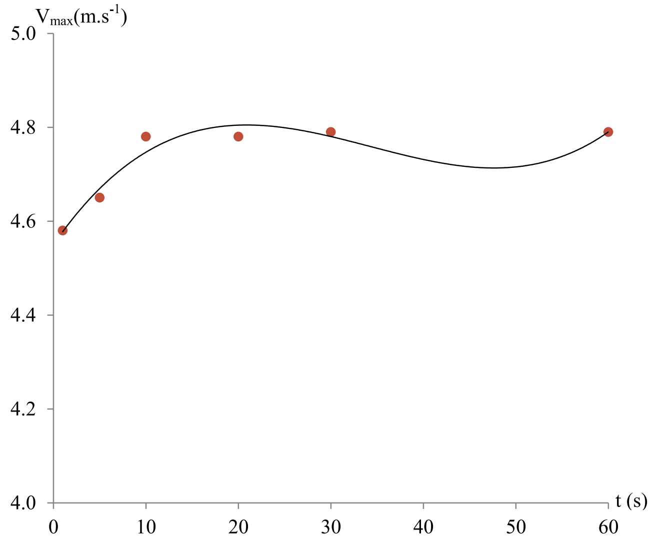

Fig. 7. Variation of the maximum value of the magnitude velocity vs. the heating time.

equations, which present the same form as the instantaneous equations. The new terms introduce the Reynolds stresses $-\rho\overline{U_i'U_j'}$ should be modeled to close the RANS equation. The used method applies the Boussinesq hypothesis relating the Reynolds stresses with the mean velocity gradients:

$$-\rho\,\overline{u'_i\,u'_j} = \mu_t\left(\frac{\partial u_i}{\partial x_j} + \frac{\partial u_j}{\partial x_i}\right) - \frac{2}{3}\left(\rho\, k + \mu_t\frac{\partial u_k}{\partial x_k}\right)\delta_{ij} \tag{3}$$

This hypothesis is undertaken in different turbulence models. This approach presents low computational cost compared to other numerical methods [29]. By using the standard k-ω turbulence model, the turbulent viscosity μ_t is defined by:

$$\mu_t = \alpha^*\frac{\rho k}{\omega} \tag{4}$$

For the correction of the low-Reynolds number, α^* is calculated as follows:

$$\alpha^* = \alpha^*_\infty\left(\frac{\alpha^*_0 + Re_t/R_k}{1 + Re_t/R_k}\right) \tag{5}$$

Where:

$$Re_t = \frac{\rho k}{\mu\omega} \tag{6}$$

$$R_k = 6 \tag{7}$$

$$\alpha^*_0 = \frac{\beta_i}{3} \tag{8}$$

$$\beta_i = 0.072 \tag{9}$$

However, for the high-Reynolds number:

$$\alpha^* = \alpha^*_\infty = 1 \tag{10}$$

For the standard k-ω turbulence model, the equations of the turbulent kinetic energy k and the specific dissipation rate ω are written as follows:

$$\frac{\partial}{\partial t}(\rho\ k) + \frac{\partial}{\partial x_i}(\rho\ k\ u_i) = \frac{\partial}{\partial x_i}\left(\Gamma_\omega\frac{\partial\, k}{\partial x_j}\right) + G_k - Y_k + S_k \tag{11}$$

$$\frac{\partial}{\partial t}(\rho\ \omega) + \frac{\partial}{\partial x_i}(\rho\ \omega\ u_i) = \frac{\partial}{\partial x_j}\left(\Gamma_\omega\frac{\partial\,\omega}{\partial x_j}\right) + G_\omega - Y_\omega + S_\omega \tag{12}$$

Constants of the standard k-ω turbulence model are presented in Table 2.

By using the concept of the Reynolds analogy [29], the energy equation is written as follows:

$$\frac{\partial}{\partial t}(\rho\ E) + \frac{\partial}{\partial x_i}[u_i(\rho\ E + p)] = \frac{\partial}{\partial x_j}\left[\left(K + \frac{c_p\,\mu_t}{Pr_t}\right)\frac{\partial\, T}{\partial x_j} + u_i(\tau_{ij})_{eff}\right] + S_h \tag{13}$$

Where E is the total energy, K is the thermal conductivity and $(\tau_{ij})_{eff}$ is the deviatoric stress tensor, defined as:

$$(\tau_{ij})_{eff} = \mu_{eff}\left(\frac{\partial\, u_j}{\partial\, x_i} + \frac{\partial\, u_i}{\partial\, x_j}\right) - \frac{2}{3}\mu_{eff}\frac{\partial\, u_k}{\partial\, x_k}\delta_{ij} \tag{14}$$

3.2. Boundary and initial conditions

For the considered box prototype, a view of the boundary conditions is presented in Fig. 3. In the first hole, the heat flow supplies the box prototype from the outside air heater, where the velocity inlet and the temperature are equal respectively to V = 3.4 m s^{-1} and T = 310 K. After that, the air flow is evacuated from the second hole of the box prototype, where the outlet pressure is equal to p = 101325 Pa. The others side surfaces of the box prototype are assumed as walls surrounding the computational domain. In these surfaces, Dirichlet boundary conditions are imposed and admit these values V = 0 m s^{-1} for the velocity and T = 290 K for the temperature. For the initial conditions, we have set all the variables to be equal V = 0 m s^{-1} for the velocity, T = 290 K for the temperature, p = 101325 Pa for the pressure and null for the turbulent characteristics. In our simulations, the time-step size is equal to t_s = 1 s. However, the number of the time-steps is equal to N_{ts} = 70 and the maximum iterations per time step are equal to N_{its} = 20000.

3.3. Meshing

Fig. 4 presents the meshing of the box prototype. In the considered application, the cells number and the nodes number are equal respectively to 167400 and 64312. This choice is done after a comparison between different meshing [30]. In fact, the numerical results are superimposed with the experimental results developed using our box prototype. The optimal mesh with good simulation results corresponds to a minimum calculated time. This choice is adopted taking into account the precision and the resolution time [25].

4. Numerical analysis

The distribution of the velocity fields, the temperature, the total pressure, the turbulent kinetic energy, the turbulence eddy frequency and the turbulent viscosity are studied over the time in the plane x = 0.06 m of the box prototype, as presented in Fig. 5. In the considered simulations, the Reynolds number is evaluated to be equal to Re = 5100.

4.1. Velocity fields

Fig. 6 shows the velocity fields in the plane x = 0.06 m containing the two holes at different instances equal to t = 1 s, t = 5 s, t = 10 s, t = 20 s, t = 30 s and t = 60 s. According to these results, it has been observed that the average velocity at the hole inlet of the box prototype

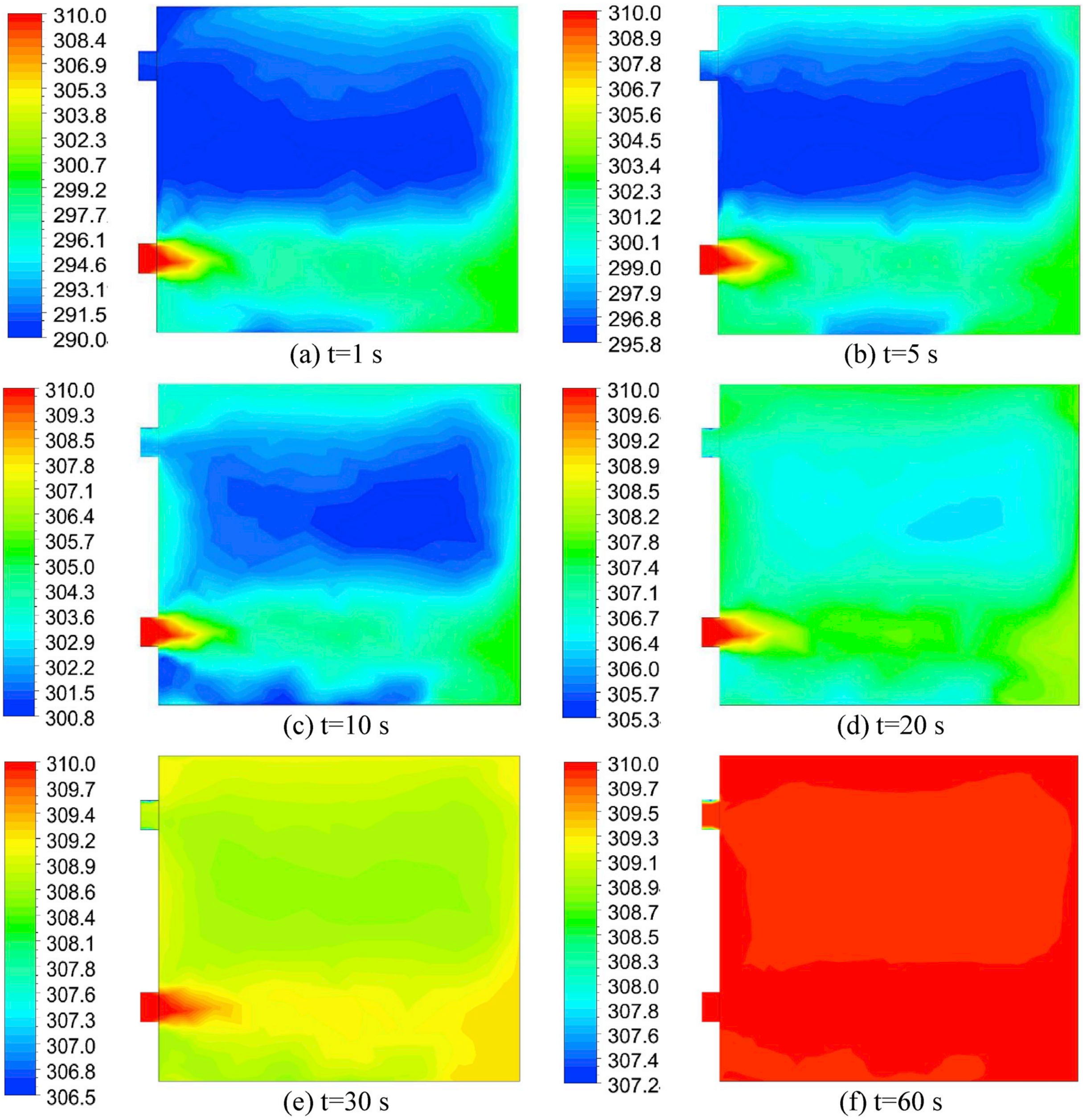

(a) t=1 s (b) t=5 s

(c) t=10 s (d) t=20 s

(e) t=30 s (f) t=60 s

Fig. 8. Distribution of the temperature in the plane defined by x = 0.06 m.

is governed by the boundary conditions and reaches $V = 3.4\,\mathrm{m\,s^{-1}}$. Indeed, a discharge area appears in the hole inlet and invaded the reverse wall. In this side, the velocity changes his direction and two axial flows have been observed. The first ascending flow is responsible for the recirculation zone appeared in the whole area of the box prototype. This movement continues until the exit of the air flow through the hole outlet. The second descending flow is the cause of the dead zone appeared in the down area. Globally, the averaged velocity value is about $V = 1.3\,\mathrm{m\,s^{-1}}$ in the discharge area. Elsewhere, the averaged velocity presents a very low value. The comparison between the founded results affirms that the maximum value of the averaged velocity increases over the time from $V = 4.58\,\mathrm{m\,s^{-1}}$ at t = 1 s to $V = 4.79\,\mathrm{m\,s^{-1}}$ at t = 60 s and reaches the steady state at this instance. These results are confirmed by Fig. 7 presenting the maximum value of the magnitude velocity over the heating time. In these conditions, the correlated equation for the considered box prototype is founded as follows:

$$V_{max} = 0.00001\,t^3 - 0.00098\,t^2 + 0.02859\,t + 4.55 \qquad (15)$$

4.2. Temperature

Fig. 8 shows the temperature distribution in the plane x = 0.06 m containing the two holes at different instances equal to t = 1 s, t = 5 s, t = 10 s, t = 20 s, t = 30 s and t = 60 s. According to these results, the temperature of the hole inlet is governed by the boundary conditions,

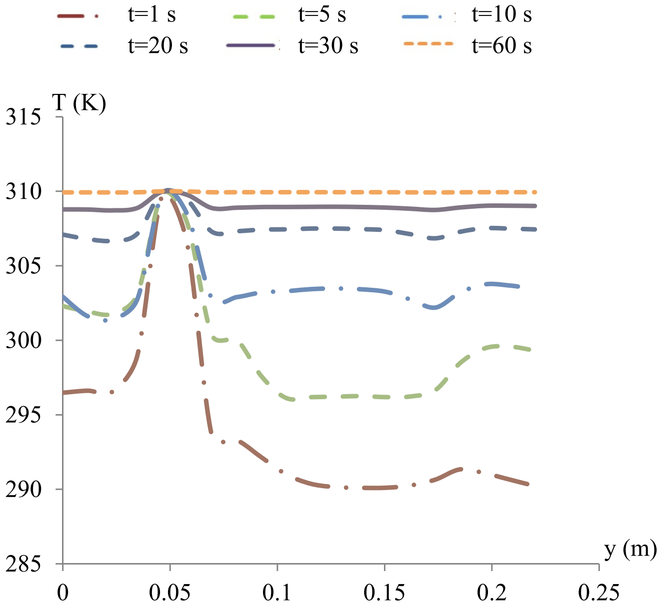

Fig. 9. Temperature profiles in the direction defined by z = −0.005 m and x = 0.06 m.

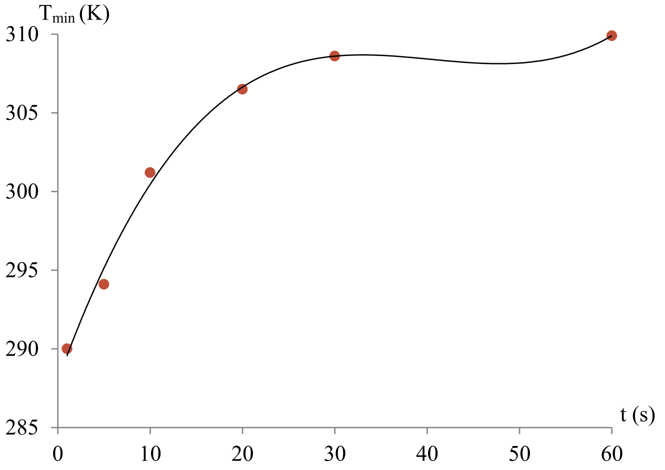

Fig. 10. Variation of the minimum value of the temperature vs. the heating time.

which is equal to T = 310 K. In the discharge area, appeared in the hole inlet and invaded until the reverse wall, it has been observed a slightly decrease of the temperature. Above the discharge area, the temperature decreases further. This fact can be explained by the recirculation zone appeared in the whole area of the box prototype. This cooling continues until the hole outlet, where the temperature presents the minimum value, depending on the heating time. For example, at t = 1 s this value reaches T = 290 K. However, this value increases over the time and reaches T = 310 K at t = 60 s, representing the steady state in this instance. From these results and as indicated in Fig. 9, presenting the temperature profile in the direction defined by z = −0.005 m and x = 0.06 m, it is clear that the box prototype requires more time and more energy to warm up. In these conditions, we confirm that the duration of 30 s is sufficient to allow the heating of the box prototype. These results are also confirmed by Fig. 10 presenting the minimum value of the temperature over the heating time. In these conditions, the correlated equation for the considered box prototype is founded as follows:

$$T_{min} = 0.0003\,t^3 - 0.0418\,t^2 + 1.6298\,t + 297.99 \qquad (16)$$

4.3. Total pressure

Fig. 11 shows the total pressure distribution in the plane x = 0.06 m containing the two holes at different instances equal to t = 1 s, t = 5 s, t = 10 s, t = 20 s, t = 30 s and t = 60 s. From these results, a compression zone emerges in the hole inlet of the box prototype. Through the air advancement, the total pressure decreases softly in the expulsion area, produced from the hole inlet and invaded until the reverse wall. This fact can be explained by the recirculation zone appeared in the whole area of the box prototype. After that, the total pressure increases to close the opposite wall and obtains the maximum value. In the hole outlet, a depression zone is observed. The comparison between the founded results affirms that the time has not affected the total pressure. In these conditions, the maximum value of the total pressure is equal to p = 101342 Pa. However, the minimum value reaches p = 101323 Pa.

4.4. Turbulent kinetic energy

Fig. 12 shows the turbulent kinetic energy distribution in the plane x = 0.06 m containing the two holes at different instances equal to t = 1 s, t = 5 s, t = 10 s, t = 20 s, t = 30 s and t = 60 s. From these results, it is noticed that the turbulent kinetic energy is stumpy in the box prototype inlet. In the expulsion area, produced in the hole inlet and invaded the reverse wall, it is observed a slight increase of the turbulent kinetic energy. The maximum value of the turbulent kinetic energy emerges in the discharge area near the reverse wall and the hole outlet of the box prototype. This fact can be explained by the recirculation zone appeared in the whole area of the box prototype. The comparison between the founded results confirms that the maximum value of the turbulent kinetic energy depends on the heating time. In fact, this value decreases from $k = 0.489\,m^2\,s^{-2}$ at t = 1 s to $k = 0.284\,m^2\,s^{-2}$ at t = 60 s and reaches the steady state at this instance.

4.5. Turbulent eddy frequency

Fig. 13 shows the turbulent eddy frequency distribution in the plane x = 0.06 m containing the two holes at different instances equal to t = 1 s, t = 5 s, t = 10 s, t = 20 s, t = 30 s and t = 60 s. From these results, it is noticed that the turbulent eddy frequency is stumpy in the box prototype inlet. In the expulsion area, produced in the hole inlet and invaded the reverse wall, it is observed a slight increase of the turbulent eddy frequency. The maximum value of the turbulent eddy frequency emerges in the discharge area near the reverse wall and the hole outlet of the box prototype. The comparison between the founded results confirms that the maximum value of the turbulent eddy frequency depends on the heating time. In fact, this value decreases from $\omega = 6197\,s^{-1}$ at t = 1 s to $\omega = 6011\,s^{-1}$ at t = 60 s and reaches the steady state in this instance.

4.6. Turbulent viscosity

Fig. 14 shows the turbulent viscosity distribution in the plane x = 0.06 m containing the two holes at different instances equal to t = 1 s, t = 5 s, t = 10 s, t = 20 s, t = 30 s and t = 60 s. From these results, it is noticed that the turbulent viscosity is stumpy in the box prototype inlet. In the expulsion area, produced in the hole inlet and

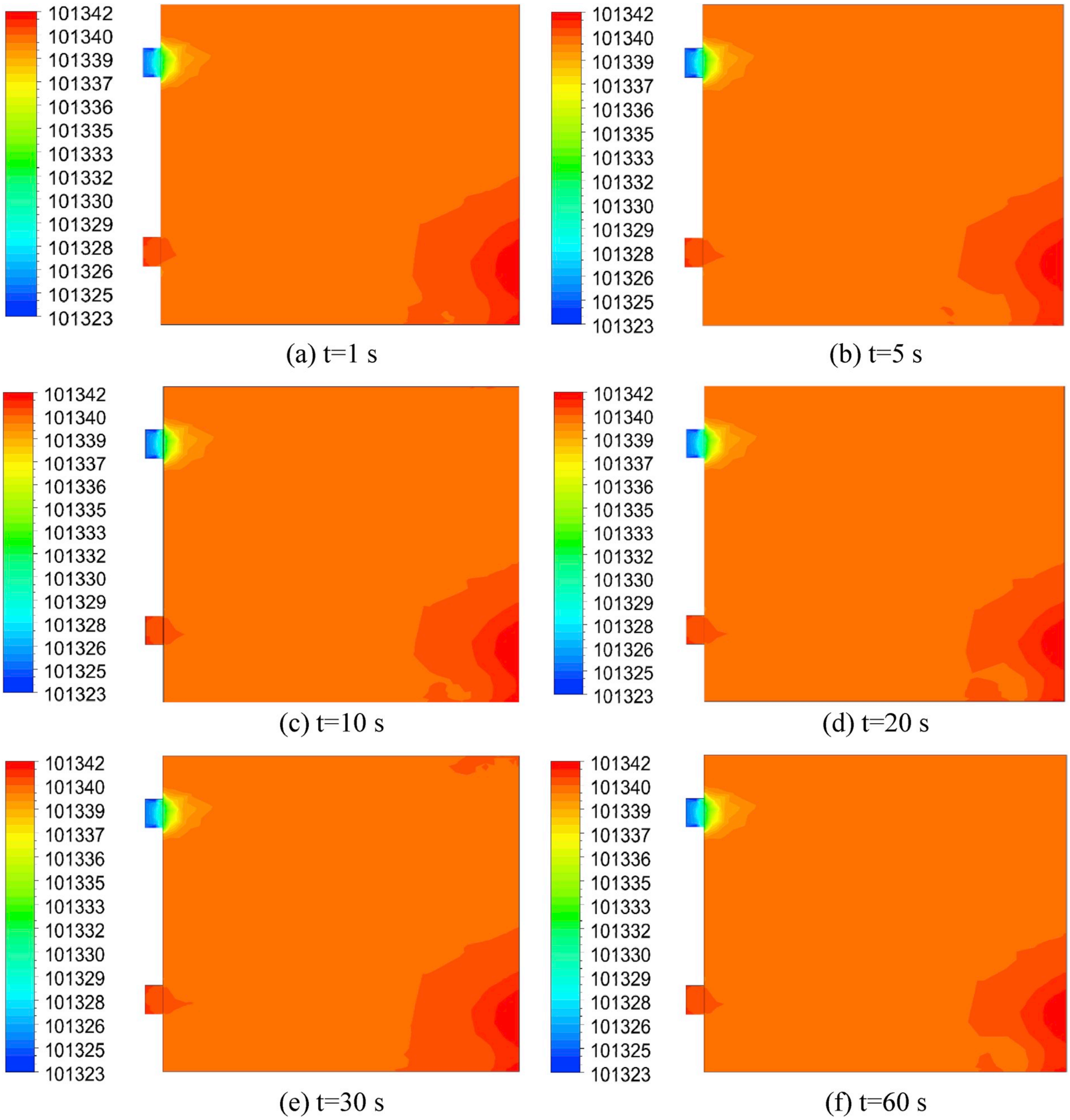

(a) t=1 s

(b) t=5 s

(c) t=10 s

(d) t=20 s

(e) t=30 s

(f) t=60 s

Fig. 11. Distribution of the pressure in the plane defined by x = 0.06 m.

invaded the reverse wall, the turbulent viscosity increases immensely. The maximum values of the turbulent viscosity emerge in the discharge area near the reverse wall and the hole outlet of the box prototype. This fact can be explained by the recirculation zone appeared in the whole area. The comparison between the founded results confirms that the maximum value of the turbulent viscosity depends on the heating time. In fact, this value decreases from $\mu_t = 0.00119\,\mathrm{kg\,m^{-1}.s^{-1}}$ at t = 1 s to $\mu_t = 0.00066\,\mathrm{kg\,m^{-1}.s^{-1}}$ at t = 60 s and reaches the steady state in this instance.

5. Comparison with experimental results

Fig. 15 shows the evolution of the velocity profiles in the direction defined by the intersection of the two planes $z = -0.005$ m and $x = 0.06$ m of the box prototype at different instances equal to t = 1 s, t = 5 s, t = 30 s and t = 60 s. From the obtained results, it is clear that the velocity presents the same profile. In these conditions, the maximum velocity value is equal to $V = 3.7\,\mathrm{m\,s^{-1}}$. Unlike the temperature profiles, time does not have a great influence on the velocity profiles variation. In fact, the velocity values slightly takedown at t = 1 s and t = 5 s. Indeed, the founded results have been confronted to the experimental data presenting the velocity profiles. Indeed, it has been noted that the value founded with the numerical model is nearest to the experimental results. In these conditions, the gap calculated between the computational and the experimental results, equal to 5%, confirms the validity of the numerical method.

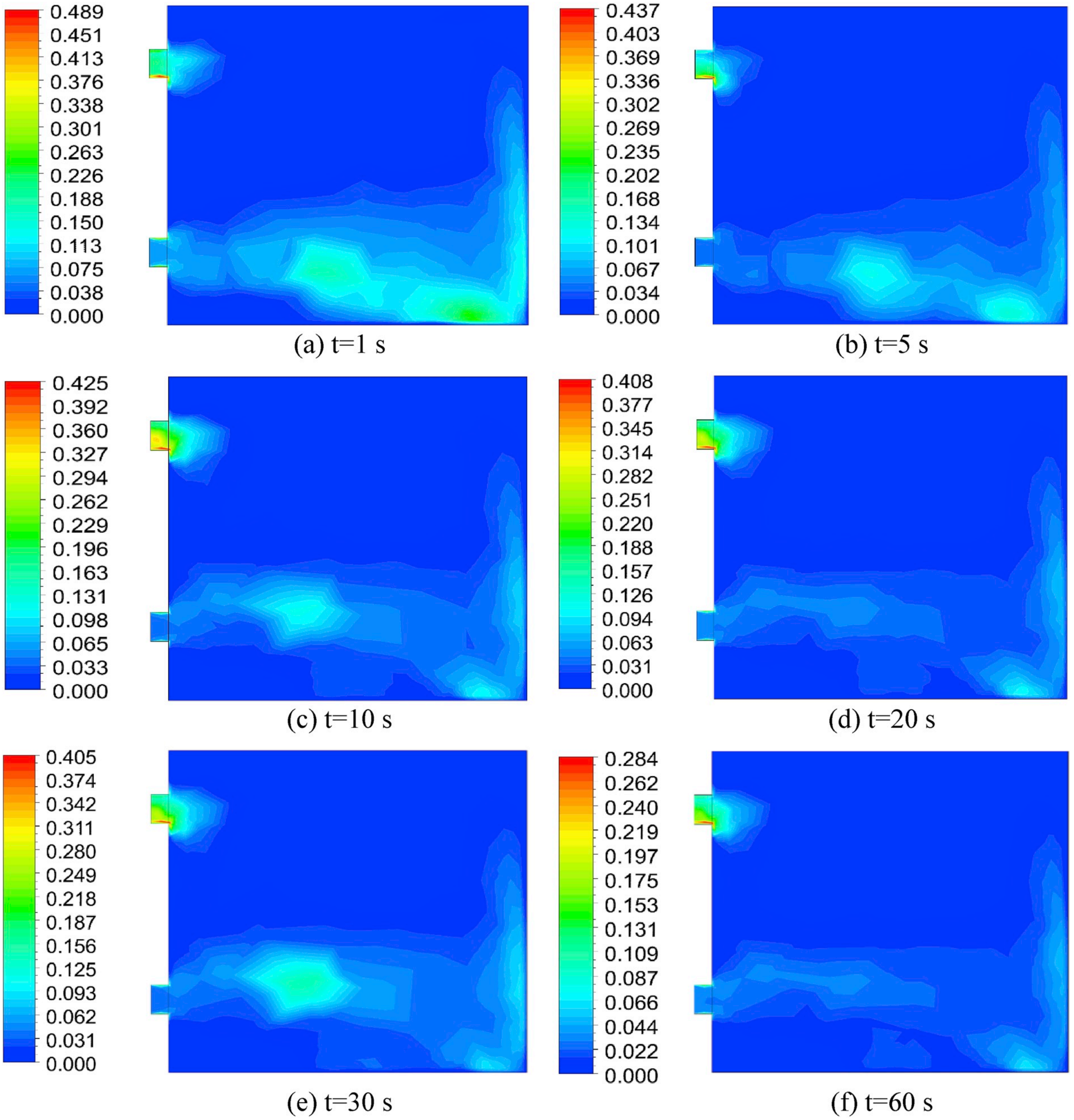

(a) t=1 s

(b) t=5 s

(c) t=10 s

(d) t=20 s

(e) t=30 s

(f) t=60 s

Fig. 12. Distribution of the turbulent kinetic energy in the plane defined by x = 0.06 m.

6. Conclusion

In this work, the impact of the unsteady state of the heat ventilation in a box prototype was investigated. The distribution of the velocity fields, the temperature, the total pressure and the turbulent characteristics were studied to characterize the aerodynamic structure of the box prototype. From these results, a discharge area appears in the hole inlet and invaded the reverse wall. In this side, the velocity changes his direction and two axial flows have been observed. The first ascending flow is responsible for the recirculation zone appeared in the whole area of the box prototype. From the hole inlet, the temperature is invaded by the reverse wall, where it has been observed a slight increase. Above the discharge area, the temperature decreases further. This heating continues until the hole outlet, where the temperature presents the minimum value depending on the heating time. The comparison between the founded results affirms that the heating time presents a straight effect on the velocity fields. In fact, the maximum value of the averaged velocity increases over the time until reaching a steady value at t = 60 s. However, for the temperature, the box prototype requires more time and more energy to warm up. In our application, we confirm that the duration of 30 s is sufficient to allow the heating of the box prototype. The comparison between the computational and the experimental results, confirms the validity of the numerical method. These results can be used in the future projects to shrink the energy consumption of the buildings and drying units.

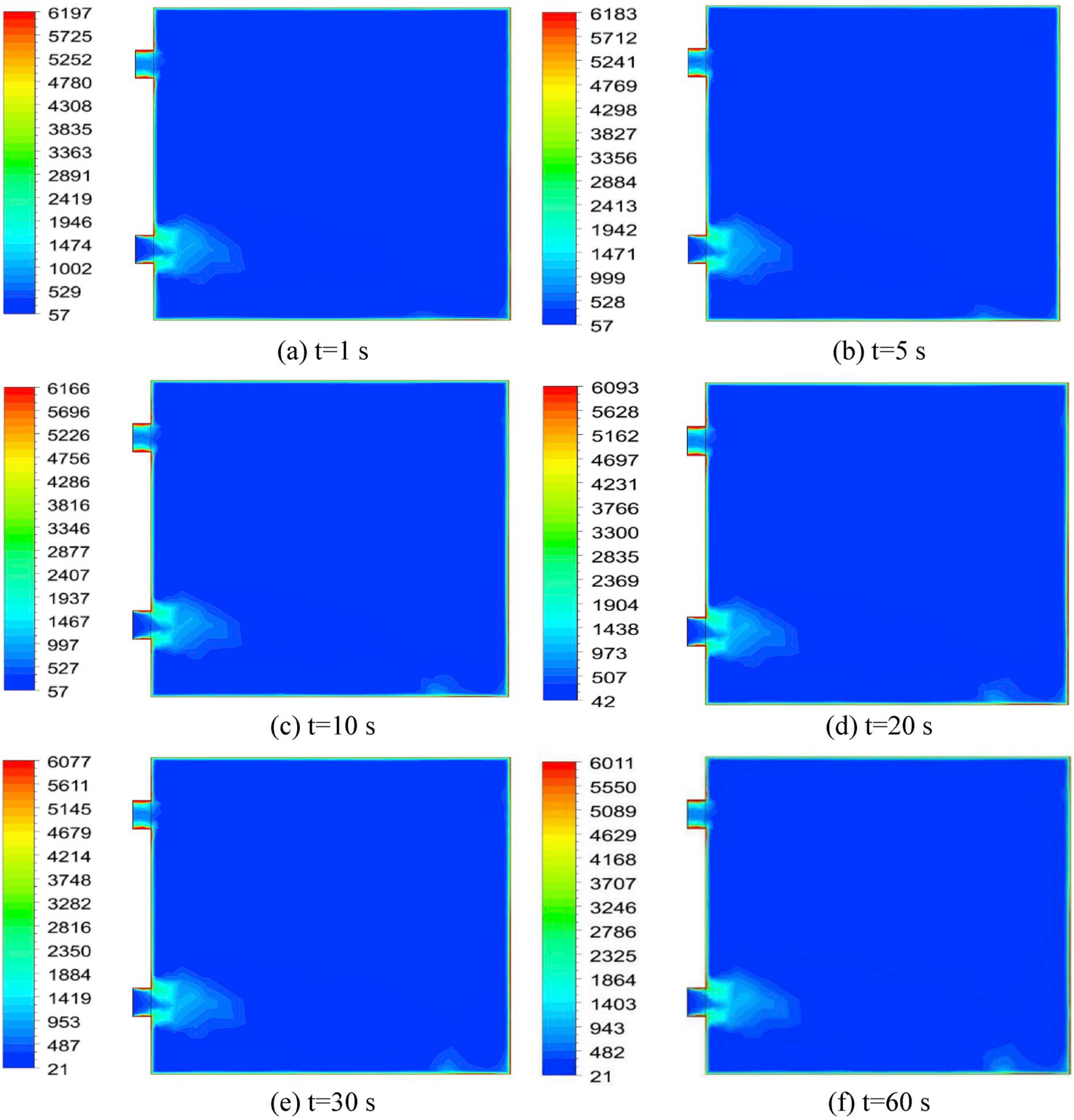

(a) t=1 s (b) t=5 s

(c) t=10 s (d) t=20 s

(e) t=30 s (f) t=60 s

Fig. 13. Distribution of the turbulence eddy frequency in the plane defined by x = 0.06 m.

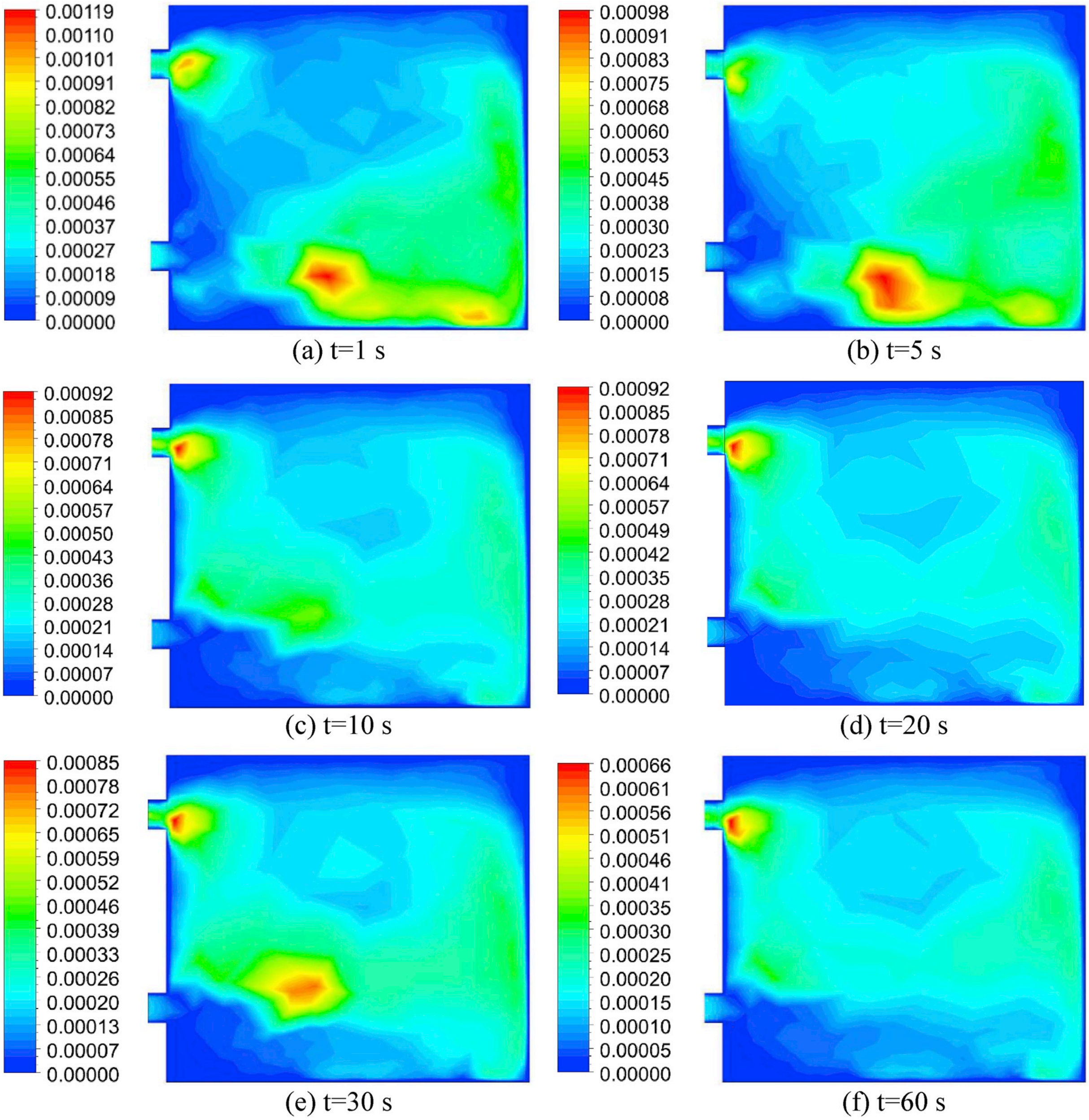

(a) t=1 s
(b) t=5 s
(c) t=10 s
(d) t=20 s
(e) t=30 s
(f) t=60 s

Fig. 14. Distribution of the turbulent viscosity in the plane defined by x = 0.06 m.

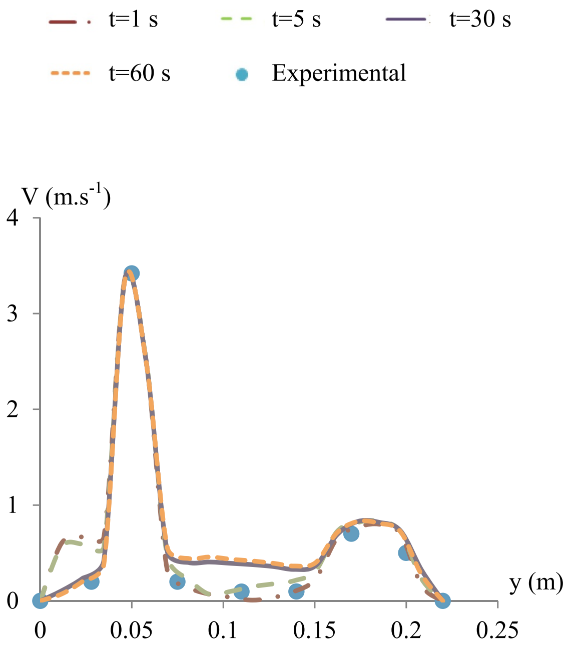

Fig. 15. Velocity profiles in the direction defined by $Z = -0.005$ m and $X = 0.06$ m.

Nomenclature

E	Total energy (J)
F_i	Force components on the i direction (N)
G_k	Generation of the turbulent kinetic energy (kg.m^{-1}.s^{-3})
G_b	Generation of turbulence kinetic energy (kg.m^{-1}.s^{-3})
G_v	Production of turbulent viscosity (kg.m.s^{-2})
G_ω	Generation of the dissipation rate of the turbulent kinetic energy (kg.m^{-1}.s^{-3})
H	Height (m)
h	Thermal enthalpy (J.kg^{-1})
k	Turbulent kinetic energy (m^2.s^{-2})
K	Thermal conductivity (W.m^{-1}. K^{-1})
L	Length (m)
N_{ts}	Number of the time-steps (dimensionless)
N_{its}	Number of maximum iterations per time step (dimensionless)
P	Pressure (Pa)
P_r	Prandt number (dimensionless)
Q_H	Heat source or sink per unit volume (kg.m^{-1}.s^{-3})
q_i	Diffusive heat flux (J)
Re	Reynolds number (dimensionless)
R_k	Constant of the k-ω turbulence model (dimensionless)
R_ω	Constant of the k-ω turbulence model (dimensionless)
S_i	Mass-distributed (kg.m^{-2}.s^{-2})
S_{ij}	Mean rate-of-strain tensor (s^{-1})
S_ω	Source terms of the specific dissipation rate of the turbulent kinetic energy (kg.m^{-1}.s^{-3})
S_k	Source terms of the turbulent kinetic energy (kg.m^{-1}.s^{-3})
T	Temperature (K)
T	Time (s)
t_s	Time-step size (s)
u	Velocity components (m.s^{-1})
u_i'	Fluctuating velocity components (m.s^{-1})
U	Free-stream velocity (m.s^{-1})
V	Magnitude velocity (m.s^{-1})
x_i	Cartesian coordinate (m)
x	Cartesian coordinate (m)
y	Cartesian coordinate (m)
Y_M	fluctuating dilatation in compressible turbulence (kg.m^{-1}.s^{-3})
Y_k	Turbulence dissipation of k (kg.m^{-1}.s^{-3})
Y_ω	Turbulence dissipation of ω (kg.m^{-1}.s^{-3})
Z	Cartesian coordinate (m)
α_0	Constant of the k-ω turbulence model (dimensionless)
α_∞	Constant of the k-ω turbulence model (dimensionless)
α_∞^*	Constant of the k-ω turbulence model (dimensionless)
δ_{ij}	Kronecker delta function (dimensionless)
μ	Dynamic viscosity (Pa.s)
μ_t	Turbulent viscosity (Pa.s)
μ_{eff}	Effective viscosity (Pa.s)
ω	Specific dissipation rate (s^{-1})
ρ	Density (kg.m^{-3})
β_i	Constant of the k-ω turbulence model (dimensionless)
σ_k	Turbulent Prandtl number for k (dimensionless)
σ_ω	Turbulent Prandtl number for ω (dimensionless)
τ_{ij}	Viscous shear stress tensor (Pa)
$(\tau_{ij})_{eff}$	Deviatoric stress tensor (Pa)
Φ	Equivalence ratio (dimensionless)
Γ_k	Effective diffusivity of k (Pa.s)
Γ_ω	Effective diffusivity of ω (Pa.s)
Ω	Swirl number (dimensionless)
Ω_{ij}	Rate of rotation tensor (s^{-1})

References

[1] L. Wang, N.H. Wong, Coupled simulations for naturally ventilated rooms between building simulation (BS) and computational fluid dynamics (CFD) for better prediction of indoor thermal environment, Build. Environ. 44 (1) (2009) 95–112.

[2] J.P. Varughese, M.M. John, Effect of emissivity of shading device and air flow inside cavity of Double Skin Facade for energy saving and Thermal Comfort in buildings: a CFD modeling, International Conference on Energy Efficient Technologies for Sustainability (2016) 815–820.

[3] S. Driss, Z. Driss, I. Kammoun, Computational study and experimental validation of the heat ventilation in a living room with a solar patio system, Energy and building 119 (2016) 28–40.

[4] S. Driss, Z. Driss, I. Kammoun, Numerical simulation and wind tunnel experiments on wind-induced natural ventilation in isolated building with patio, Energy 90 (2015) 917–925.

[5] A. Rauf, R.H. Crawford, Building service life and its effect on the life cycle embodied energy of buildings, Energy 79 (2015) 140–148.

[6] M. Premrov, V.Z. Leskovar, K. Mihalic, Influence of the building shape on the energy performance of timber-glass buildings in different climatic conditions, Energy 108 (2016) 201–211.

[7] Z. Zhang, W. Zhang, Z.J. Zhai, Q.Y. Chen, Evaluation of various turbulence models in predicting airflow and turbulence in enclosed environments by CFD: Part 2 Comparison with experimental data from literature, HVAC R Res. 13 (6) (2007) 871–886.

[8] B. Soni, S. Aliabadi, Large-scale CFD simulations of airflow and particle deposition in lung airway, Comput. Fluids 88 (2013) 804–812.

[9] P. Evegren, J. Revstedt, L. Fuchs, Pulsating flow and mass transfer in an asymmetric system of bifurcations, Comput. Fluids 49 (2011) 46–61.

[10] R.K. Calay, J. Kurujareon, A.E. Holdø, Numerical simulation of respiratory flow patterns within human lung, Respir. Physiol. Neurobiol. 130 (2002) 201–221.

[11] O. Aydm, Transient natural convection in rectangular enclosures heated from one side and cooled from above, Int. Commun. Heat Mass Tran. 26 (1999) 135–144.

[12] S.W. Baek, T.Y. Kim, Effects of surface radiation on the unsteady natural convection in a rectangular enclosure, International Journal of Aeronautical and Space Sciences 3 (2002) 95–104.

[13] Z.J. Zhu, H.X. Yang, Numerical investigation of transient laminar natural convection of air in a tall cavity, Heat Mass Tran. 39 (2003) 579–587.

[14] J.H. Bae, J.M. Hyun, Time-dependent buoyant convection in an enclosure with discrete heat sources, Int. J. Therm. Sci. 43 (2004) 3–11.

[15] I. Kurtbas, A. Durmus, Unsteady heat transfer by natural convection in the cavity of a passive heating room, Int. J. Therm. Sci. 47 (2008) 1026–1042.

[16] I.A. Aleshkova, M.A. Sheremet, Unsteady conjugate natural convection in a square enclosure filled with a porous medium, Int. J. Heat Mass Tran. 53 (23–24) (2010) 5308–5320.

[17] W. Zhang, C. Zhang, G. Xi, Conjugate conduction-natural convection in an enclosure with time-periodic sidewall temperature and inclination, Int. J. Heat Fluid Flow 32 (2011) 52–64.

[18] S.G. Martyushev, M.A. Sheremet, Conjugate natural convection combined with surface thermal radiation in an air filled cavity with internal heat source, Int. J. Therm. Sci. 76 (2014) 51–67.

[19] F. Noh-Pat, J. Xamán, G. Álvarez, M. Gijón-Rivera, I. Hernández-Pérez, J. Arce, E. Villanueva-Vega, Unsteady-RANS simulation of conjugate heat transfer in a cavity with a vertical semitransparent wall, Comput. Fluids 117 (2015) 183–195.

[20] J.M. Armengol, F.C. Bannwart, J. Xamán, R.G. Santos, Effects of variable air

properties on transient natural convection for large temperature differences, Int. J. Therm. Sci. 120 (2017) 63–79.

[21] M.A. Sheremet, I. Pop, A. Ishak, Time-dependent natural convection of micropolar fluid in a wavy triangular cavity, Int. J. Heat Mass Tran. 105 (2017) 610–622.

[22] I. Yılmaz, H.F. Öztop, Turbulence forced convection heat transfer over double forward facing step flow, Int. Commun. Heat Mass Tran. 33 (2006) 508–517.

[23] F. Selimefendigil, H.F. Öztop, K. Al-Salem, Natural convection of ferrofluids in partially heated square enclosures, J. Magn. Magn Mater. 372 (2014) 122–133.

[24] H.F. Oztop, C. Sun, B. Yu, Conjugate-mixed convection heat transfer in a lid-driven enclosure with thick bottom wall, Int. Commun. Heat Mass Tran. 35 (2008) 779–785.

[25] Z. Driss, O. Mlayeh, D. Driss, M. Maaloul, M.S. Abid, Numerical simulation and experimental validation of the turbulent flow around a small incurved Savonius wind rotor, Energy 74 (2014) 506–517.

[26] Z. Driss, O. Mlayeh, D. Driss, M. Maaloul, M.S. Abid, Numerical simulation and experimental validation of the turbulent flow around a small incurved Savonius wind rotor, Energy 74 (2014) 506–517.

[27] Z. Driss, O. Mlayah, S. Driss, D. Driss, M. Maaloul, M.S. Abid, Study of the bucket design effect on the turbulent flow around unconventional Savonius wind rotors, Energy 89 (2015) 708–729.

[28] Z. Driss, O. Mlayah, S. Driss, M. Maaloul, M.S. Abid, Study of the incidence angle effect on the aerodynamic structure characteristics of an incurved Savonius wind rotor placed in a wind tunnel, Energy 113 (2016) 894–908.

[29] ANSYS Fluent Theory Guide, ANSYS, Inc, Southpointe 2600, ANSYS Drive Canonsburg, PA, 2016, p. 15317.

[30] B. Bakri, S. Driss, A. Ketata, H. Benguesmia, F. Hamrit, Z. Driss, Study of the meshing effect on the turbulent flow in a building system with a k-ω turbulence model. International Conference on Mechanics and Energy (ICME'2016), December 22-24 2016, Hammamet, Tunisia.